Validation of a flow-structure-interaction computation model of phonation

Pinaki Bhattacharya, Thomas Siegmund*

School of Mechanical Engineering, Purdue University, West Lafayette, IN 47907 USA

Summary: Computational models of vocal fold (VF) vibration are becoming increasingly sophisticated, their utility currently transiting from exploratory research to predictive research. However, validation of such models has remained largely qualitative, raising questions over their applicability to interpret clinical situations. In this paper, a computational model with a segregated implementation is detailed. The model is used to predict the fluid–structure interaction (FSI) observed in a physical replica of the VFs when it is excited by airflow. Detailed quantitative comparisons are provided between the computational model and the corresponding experiment. First, the flow model is separately validated in the absence of VF motion. Then, in the presence of flow-induced VF motion, comparisons are made of the flow pressure on the VF walls and of the resulting VF displacements. Self-similarity of spatial distributions of flow pressure and VF displacements is highlighted. The self-similarity leads to normalized pressure and displacement profiles. It is shown that by using linear superposition of average and fluctuation components of normalized computed displacements, it is possible to determine displacements in the physical VF replica over a range of VF vibration conditions. Mechanical stresses in the VF interior are related to the VF displacements, thereby the computational model can also determine VF stresses over a range of phonation conditions.

Key Words: vocal fold, self-oscillation, computer model, validation

1. Introduction

The myoelastic–aerodynamic theory of phonation (van den Berg, 1958; Titze, 2006) states that phonation is a result of two sources of oscillatory behavior. The first source (myoelastic) is based on the muscular nature of the VF tissue. It causes self-sustained oscillations in a similar manner as the elasticity in a spring causes the spring to vibrate (indefinitely in the absence of friction) when displaced from its resting state. The second source (aerodynamic) is based on the variation in fluid pressure associated with flow passing through a duct of varying cross-sectional geometry. This source causes the VFs to vibrate by creating regions of varying

*Corresponding author
Email address: siegmund@purdue.edu (Thomas Siegmund)

wall-pressure – and thus regions of relative push/pull – which in turn are cause by the airflow undergoing significant constriction in the glottis and a sudden expansion in the supra-glottal tract. Thus phonation is a result of cyclic imbalance between glottal air flow pressure and muscular tension in the vocal folds (VFs). Computational models of this flow–structure interaction (FSI) between glottal air flow and VFs are becoming increasingly realizable (de Oliveira Rosa et al., 2003; Alipour and Scherer, 2004; Thomson et al., 2005; Decker and Thomson, 2007; Luo et al., 2008, 2009; Zheng et al., 2009, 2010; Mittal et al., 2011; Bhattacharya and Siegmund, in press) with the rapid advance in computation power and availability of sophisticated numerical algorithms. As an attractive alternative to excised and synthetic VF models, computational models provide unique advantages: (i) models are non-destructive and non-interfering, (ii) can be used to remove confounding factors (by abstraction) and (iii) can be used in sensitivity analysis (by parametric variation). A particular advantage is that computational models can be used to directly determine mechanical stresses in the VF interior. This unique capability is very important in understanding VF health, which depends on the state of stress within the VF (Titze, 1994; Chan and Tayama, 2002; Leydon et al., 2009). Design of VF implants (Zeitels et al., 2003) and investigation of glottal tract abnormalities e.g. subglottic stenosis (Smith and Thomson, 2013) would also benefit significantly from validated results. Notwithstanding the advances in the state-of-the-art of computer models, the validation of such models with experiment has been largely qualitative. The detailed quantitative validation of a computer model of VF vibration is the focus of the present study.

In FSI computations, the main challenges are (i) the dissimilar conventions in the description of the flow and VF domains (Eulerian and Lagrangian respectively), (ii) the necessity of tracking the flow-structure interface requiring complex discretization strategies and management of physical variables on the interface, (iii) the three-dimensionality of both domains, (iv) the complex constitutive behavior of VF tissue, and (v) the stability and accuracy issues in transient solvers of both physical domains. Though the preceding list applies strictly to implementations with separate fluid and structural solvers (segregated implementations), in alternative implementations with a single solver (monolithic implementations) some of the above challenges are overcome but only at the cost of additional complexities. Further, in both segregated and monolithic implementations, simulation of the minimum interval of interest in physical time typically requires computations to run for times that are larger than the physical time by orders of magnitude.

The foregoing computational challenges necessitate simplifications or restrictive assumptions in order to ensure the feasibility of the computational effort. Since simplifications will limit the validity of a particular model, the relevance of each restriction or simplification must be evaluated in the context of the study. For instance, two-dimensional studies, though computationally inexpensive, cannot provide insights into the three-dimensional (3D) nature of the glottal jet. Another motivation to include a particular simplification is to remove confounding factors within the physical problem. There are several aspects to the interaction between the airflow and the VFs (e.g. acoustics, glottal jet dynamics, VF wall motion, stresses within VF,

VF hydration, etc.). Depending on the focus of a particular research study, the formulation of certain aspects will be more detailed than others. Though it is obvious that different aspects of the problem interact, it is not always clear to what degree they do. Therefore, approximations made to simplify a certain aspect (computational or physical) must be carefully analysed for the effect they have on the focus of the study.

The aim of the present paper is to validate VF deformations computed from a 3D computational model of self-sustained VF vibrations. It has been shown that the model can be extended to include aspects of VF collision and complex constitutive behavior of the VFs (Bhattacharya and Siegmund, in press). Commercially available solvers are employed to facilitate model development (complex geometry, constitutive properties, discretization and coupling) and to leverage post-processing capabilities. The model can be deployed on parallel processors, thereby increasing computation speed.

Existing experimental techniques do not allow the determination of mechanical strains in the VF interior vibration (Mittal et al., 2013). However, optical measurements of the superior surface displacements during free vibration are readily possible and used here in the computation–experiment comparison. This choice of validation strategy has the following motivation. In an elastic-viscoelastic solid continuum like the VFs, the stresses are completely determined if the strains and strain-rates are known. Therefore, validation of displacements, which determines strains and strain-rates, is sufficient to validate stresses within the VFs. Detailed displacement measurements have been obtained during free vibration on the VF superior surface (Wittenberg et al., 2000; Spencer et al., 2008; George et al., 2008; Chen, 2009).

The validation strategy is further enhanced by separately considering flow studies. The underlying rationale for this approach is that the airflow is the sole source of energy available to the VF for generating motion. The interaction between the VFs and glottal flow takes place through the energy transfer across the glottal surface. Both normal tractions (or flow pressures) and shear tractions arise on the glottal surface (Alipour and Scherer, 2004), but there is sufficient evidence that the predominant mode of energy transfer is due to the flow pressures (Thomson et al., 2005). Therefore a validation of computed flow pressures is included. However, no experimental data on flow pressures on the VF surface during FSI are available due to the challenges in obtaining such measurements. Thus, a direct validation of computed flow pressures in vibrating VFs is infeasible. Accordingly, the flow validation strategy is adapted as follows. Firstly, the flow-domain model within the segregated FSI model is separately exercised for the case of rigid VFs. Computed flow pressures are then compared with those obtained from a rigid VF experiment. Secondly, a comparison is made between flow pressures obtained from experiments on rigid VFs resembling instantaneous deformed VF shapes and those obtained from the full FSI computation with vibrating VFs. In previous experimental studies with rigid VF glottal shapes resembling instantaneous deformed VF shapes (Guo and Scherer, 1993; Scherer et al., 2001, 2002; Shinwari et al., 2003; Scherer et al., 2010; Fulcher et al., 2010) flow pressure on the VF walls have been reliably obtained. Such studies were motivated by the quasi-steady approximation (McGowan, 1993), which states that the instantaneous flow field though a vibrating glottis

is not significantly altered if the deformation of the glottis is frozen in time. It must also be remarked that a considerable body of work exists on computation of glottal airflow past rigid VFs. With respect to VF wall pressures, these studies have shown excellent correspondence with experimental measurements, even when including significant variation in VF geometry (Guo and Scherer, 1993; Scherer et al., 2001, 2002, 2010; Li et al., 2006a; Fulcher et al., 2011; Li et al., 2012). This branch of investigation has clearly demonstrated the sensitivity of flow pressure development to changes in VF geometry and hence to VF motion. In this paper wall pressure profiles computed on deformed VFs shapes (attained during FSI) are sometimes validated by comparing with computed flow pressures on rigid VF walls with similar geometry as reported in literature. However such comparisons are made sparingly and only when experimental measurements for a corresponding deformed VF geometry are unavailable. The comparison between FSI computed flow pressures and flow pressures (measured or computed) on rigid VFs resembling instantaneous deformed VF shapes provides insight into the applicability of the quasi-steady approximation.

For direct comparison of displacement fields between computed results and experimental observations it is necessary to excite the VFs at the same flow conditions as present in the experiment. However, normal phonation usually spans a range of flow-conditions. Further, given the cost of running computer simulations with continuum models of 3D self-oscillating VFs, it is cost-prohibitive to separately validate the model for a range of flow conditions. Therefore, in this paper, a normalization strategy based on linear superposition principle is introduced. The motivation for this particular normalization comes from experimental evidence that during normal phonation vibration-induced strains on the VF tissue are sufficiently small for non-linear strain effects to be ignored. Thereby, it is assumed that the total displacement field of the VF during vibration can be decomposed into a mean component and a fluctuation component. The mean VF displacement (and thus the mean VF deformed shape) normalized by the mean transglottal pressure difference (TPD) is hypothesized to be self-similar. The TPD is the difference between levels of flow pressure at inlet and outlet. Thus, for a physical VF model, the mean deformed shape during vibration can be predicted using the normalized deformed shape obtained from computation, with the condition that the mean TPD in the physical experiment is known. Furthermore, experimentally obtained images of VF motion (Spencer et al., 2008; George et al., 2008; Chen, 2009) lead to the insight that all locations within the VF domain follow a single harmonic dependence on time with respect to the fluctuation component of displacement. Thus, the spatial variation of the fluctuation displacement component, normalized by the fluctuation displacement at a given point, is expected to be self-similar when compared at different instants of time. A location on the VF superior surface is a good choice for normalizing the fluctuation displacement component as reliable techniques have already been developed in previous research to measure VF superior surface displacements (Spencer et al., 2008; George et al., 2008; Chen, 2009).

If the above hypotheses on the self-similarity of displacements hold, and the corresponding scaling factors are known, it immediately follows that the computed vibration response of the VF can be used to predict

the spatio-temporal variation of displacement. Since stresses are completely determined from derivatives of displacements, the spatio-temporal variation of stresses in the VF interior can be predicted as well. The quantitative validation is then complete for all locations within the VF once it is established that the normalized mean and fluctuation displacement components match between computation and experiment.

2. Method

2.1. Computational Models

The governing equations for the flow domain are given by

$$\oint_{\partial(V^f)} (\vec{v} - \vec{v}_\mathrm{g}) \cdot \mathrm{d}\vec{S} = 0, \tag{1}$$

$$\rho_\mathrm{f} \frac{\mathrm{d}}{\mathrm{d}t} \int_{V^f} \vec{v}\, \mathrm{d}V + \rho_\mathrm{f} \oint_{\partial(V^f)} \vec{v}\, (\vec{v} - \vec{v}_\mathrm{g}) \cdot \mathrm{d}\vec{S} = - \oint_{\partial(V^f)} p\boldsymbol{I} \cdot \mathrm{d}\vec{S} + \oint_{\partial(V^f)} \boldsymbol{\tau}_\mathrm{f} \cdot \mathrm{d}\vec{S}, \tag{2}$$

where V^f denotes the volume of the entire flow domain, $\partial(V^f)$ is its bounding surface, $\vec{v}$ is the velocity of a fluid particle, $\vec{v}_\mathrm{g}$ is the velocity of the grid points comprising the discretized domain, $\rho_\mathrm{f} = 1.23$ kg/m^3 is the density of the fluid (air), t denotes time, p is the static pressure due to the flow (with respect to a reference pressure $p_\mathrm{ref} = 1.01$ kPa) and $\boldsymbol{I}$ is the second-order identity tensor. The relation

$$\boldsymbol{\tau}_\mathrm{f} = \mu \left[\nabla \vec{v} + (\nabla \vec{v})^T \right], \tag{3}$$

describes the constitutive behavior of the fluid, where $\boldsymbol{\tau}_\mathrm{f}$ is the stress tensor on the fluid particle, $\mu = 1.79 \cdot 10^{-5}$ kg/m·s is the dynamic vicosity of the fluid, superscript T refers to transpose and ∇ is the gradient operator. Constitutive properties (ρ_f and μ) corresponding to that of air at STP are imposed (Table 2).

2.1.1. Computational Model with Rigid Vocal Folds

In the rigid VF model, the glottal surface geometry is considered to be two-dimensional. In voice literature a class of generic glottal shapes called M5 is well-known (Scherer et al., 2001). In the present model the glottal profile corresponds to an M5 geometry with included glottal angle of 10° (divergent), a glottal obliquity of 0° and a minimum glottal diameter $d_\mathrm{g} = 0.4$ mm. This particular glottal profile along with sub- and supra-glottal tracts comprises the computational flow domain (Fig. 1). The mesh is similar to that in Suh and Frankel (2007) where the smallest edge length is of the order 0.002 mm. The VF surface does not deform at any point in time. Thereby, the grid velocity $\vec{v}_\mathrm{g}$ is identically zero everywhere. Following 2D definition, all vector-valued variables have components in the mutually-perpendicular inferior–superior and medial–lateral directions. The coordinates in the inferior–superior and medial–lateral directions are referred to as x_is and x_ml respectively. At the inlet and the outlet constant pressure values are specified,

$$\begin{aligned} \text{inlet}: &\qquad p(x_\mathrm{is} = -T_\mathrm{entry} - T) = p_\mathrm{max}, \\ \text{outlet}: &\qquad p(x_\mathrm{is} = T_\mathrm{exit}) = 0. \end{aligned} \tag{4}$$

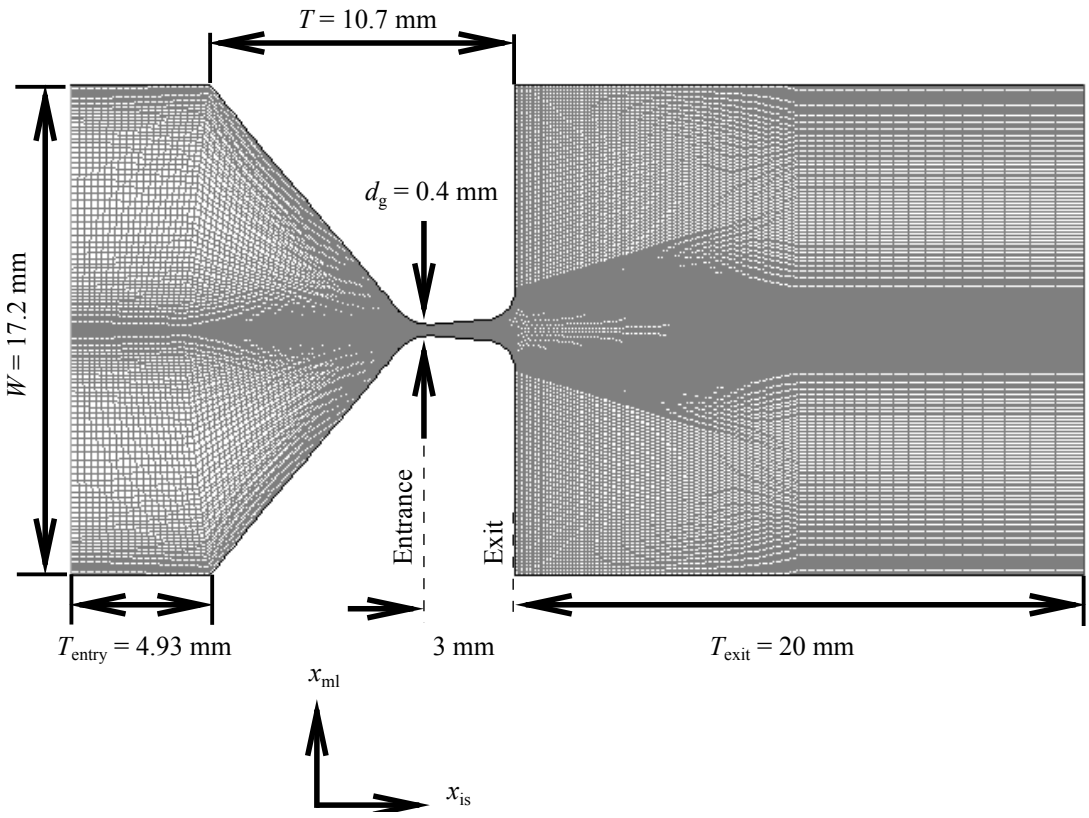

Figure 1: Mesh of two-dimensional airflow domain in the rigid vocal fold model. The glottal shape shown here is identical to any coronal section of the experimental model in Scherer et al. (2001).

At all the remaining flow-domain boundaries the no-slip condition is specified,

$$\vec{v} = \vec{v}_g \equiv 0. \tag{5}$$

Note that with the outlet pressure level set to zero, the TPD at any instant is identical to the inlet pressure level. Two sets of computations were performed, with inlet pressure levels $p_{\max}$ equal to 3.00 cm water (294 Pa) and 15.0 cm water (1470 Pa). These values span the range investigated in Scherer et al. (2001). The PRESTO! algorithm is used to discretize the pressure variables, a first-order upwind method is used for the velocity variables, and the PISO procedure is followed to integrate the governing equations in time. The time-integration procedure is first-order implicit. The flow computation is performed with a fixed time-increment of $\Delta t = 1 \times 10^{-5}$ s until a steady state is achieved.

2.1.2. Computational Model with Flexible Vocal Folds

In the flexible VF computational model the geometry is considered to be three-dimensional. The model comprises separate continuum definitions for the glottal airflow domain (Fig. 2a) and the pair of VF tissue domains (one VF is shown in Fig. 2b). The model also includes a formulation for the interaction between the

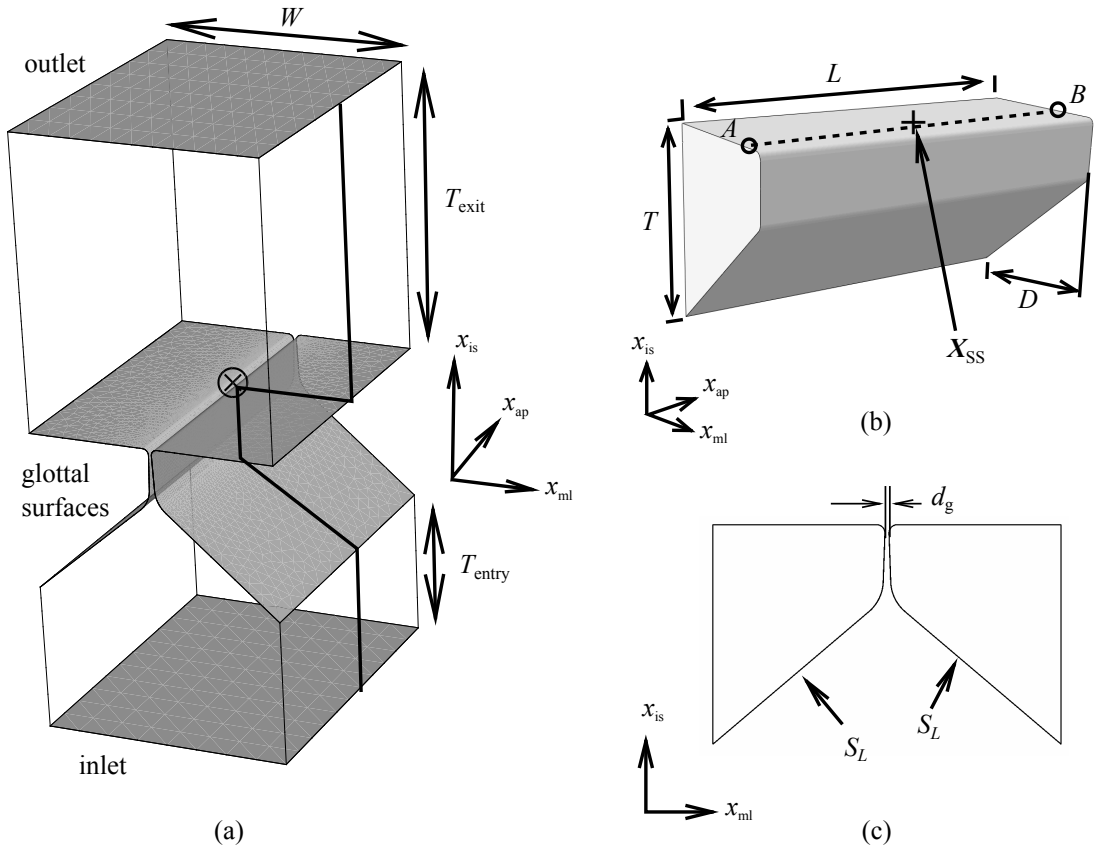

Figure 2: (a) Geometry of the glottal airflow domain. The inlet, outlet and glottal surfaces are shaded. The coordinate origin is denoted by $\otimes$. (b) Geometry of the left half of the VF model. (c) Mid-coronal section showing pair of VFs. Coordinate axes are offset from the origin for clarity.

air (fluid) and VF tissue (structural) domains. In the 3D model, x_{ap} denotes the anterior-posterior coordinate and a right-hand coordinate system is fixed by choosing the x_{is}, x_{ml} and x_{ap} axes. The coordinate system origin located at the intersection of the mid-coronal plane, the mid-saggital plane and the (planar) VF superior surface. Dimensions of the fluid and VF domains are given in table 1. The differences between model geometries of the flexible VF model and the rigid VF model are as follows. The glottal profile in the flexible VF model has an included angle of -2° (convergent). The inlet tract used in the flexible VF model is longer than that in the rigid VF model. Finally, the minimum glottal diameter d_{g} (Fig. 2c) is smaller in the flexible VF model compared to that in the rigid VF model. However, note that the minimum glottal diameter d_{g} and intra-glottal angle are specified only in the initial pre-phonatory configuration. As the VF motion develops in time, both the minimum glottal diameter and intra-glottal angle are expected to change.

Equations (1)–(3) continue to describe the governing equations and constitutive relationship for the flow domain, except that now the vector-valued variables have three components. The pressure at the inlet

Table 1: Dimensions of 3D computational model with flexible VFs

T_{entry}	10.0 mm	T_{exit}	20.0 mm
d_{g}	0.200 mm	L	22.0 mm
W	17.0 mm	T	10.7 mm
D	8.40 mm		

surface is specified as

$$p(x_{\text{is}} = -T_{\text{entry}} - T) \equiv p_{\text{in}}(t) = p_{\max} \begin{cases} (t/t_{\text{ramp}})^2[3 - 2(t/t_{\text{ramp}})] & \forall t \in [0, t_{\text{ramp}}] \\ 1 & \forall t \in [t_{\text{ramp}}, \infty). \end{cases} \tag{6}$$

A maximum inlet pressure level $p_{\max} = 300$ Pa was attained after a ramp period $t_{\text{ramp}} = 0.100$ s. The pressure at the outlet is fixed at zero,

$$p(x_{\text{is}} = T_{\text{exit}}) = 0. \tag{7}$$

At all the remaining flow-domain boundaries the no-slip condition is specified,

$$\vec{v} = \vec{v}_{\text{g}}. \tag{8}$$

The grid velocity v_g is zero at the anterior–posterior and medial–lateral bounding surfaces,

$$\vec{v}_{\text{g}}(x_{\text{ml}} = \pm W/2) = 0, \tag{9}$$

$$\vec{v}_{\text{g}}(x_{\text{ap}} = \pm L/2) = 0. \tag{10}$$

The fluid volume is discretized using tetrahedral cells with a minimum cell size of 0.050 mm near the glottis. Remeshing is performed after every time increment. Suitable size functions are employed which ensure that in the near glottis region the minimum cell size is maintained throughout the computation. The discretization of variables and time-integration procedure is identical to that for the rigid VF model.

Table 2: Constitutive properties used in the flexible VF computational model.

ρ_{s}	1070 kg/m^3	E	6.00 kPa	ν	0.450
τ_1	0.100 s	k_1	0.100	g_1	0.100

The governing equation for each VF structure is

$$\int_{V^s} \boldsymbol{\sigma} : \delta \boldsymbol{D}_{\text{v}} \, \mathrm{d}V = \oint_{\partial(V^s)} \vec{\tau}_{\text{s}} \cdot \delta \vec{u}_{\text{v}} \, \mathrm{d}S - \int_{V^s} \rho_{\text{s}} \ddot{\vec{u}} \cdot \delta \vec{u}_{\text{v}} \, \mathrm{d}V, \tag{11}$$

supplemented by the boundary conditions

$$\vec{u}(x_{\text{ap}} = \pm L/2) = 0, \qquad \vec{u}(x_{\text{ml}} = \pm W/2) = 0, \tag{12}$$

which constrain the anterior, posterior and lateral VF surfaces. Here, $\boldsymbol{\sigma}$ is the Cauchy stress tensor for the VF domain, $\vec{\tau}_{\rm s}$ is a surface traction vector, $\rho_{\rm s}$ is the density of the VF tissue, $\vec{u}$ and $\ddot{\vec{u}}$ are respectively the displacement and acceleration vectors associated with a material point, $\delta\vec{u}_{\rm v}$ is a virtual displacement (vector) and $\delta\boldsymbol{D}_{\rm v}$ is the corresponding virtual strain tensor. The VFs are considered to be linear elastic isotropic with viscoelastic behavior. The following equations

$$\boldsymbol{\sigma}(t) = \int_0^t 2G(t-t')\dot{\boldsymbol{e}}\,\mathrm{d}t' + \boldsymbol{I}\int_0^t K(t-t')\dot{\epsilon}\,\mathrm{d}t' \tag{13}$$

$$G(t) = \frac{E}{2(1+\nu)}\left[1-g_1+g_1\mathrm{e}^{-t/\tau_1}\right], \tag{14}$$

$$K(t) = \frac{E}{(1-2\nu)}\left[1-k_1+k_1\mathrm{e}^{-t/\tau_1}\right], \tag{15}$$

describe the constitutive relations for the VF tissue, where $\boldsymbol{e}$ is the deviatoric strain tensor and ϵ is the volumetric strain. The elastic modulus for the VF tissue is E and the Poisson's ratio is ν, and functions G and K describe respectively the shear and bulk modulus relaxation with time. Respective constitutive properties are given in table 2. The VF volumes are discretized using 3D continuum hexahedral elements with minimum edge length 0.110 mm near the medial surface. The time integration of (11) is carried out with a fixed time-step of $\Delta t = 1\times10^{-5}$ s using the Hilber-Hughes-Taylor dynamic implicit algorithm with relaxation parameter $\alpha = -0.41421$. The inferior–superior and medial–lateral displacement components at points along an anterior–posterior oriented line on the left VF superior surface were extracted. This line, henceforth referred to as AB is shown in Fig. 2b in the VF reference state. It is offset by 1.50 mm from the VF medial surface. The mid-coronal plane intersects line AB at $\vec{X}_{\rm SS}$. The displacements along line AB were considered to be representative of the overall VF deformation.

Interaction conditions on the glottal surfaces of the structural and fluid domains are given by

$$\vec{v}_{\rm g} = \dot{\vec{u}} \quad \text{and} \quad \vec{\tau}_{\rm s} = (-p\boldsymbol{I}+\boldsymbol{\tau}_{\rm f})\cdot\hat{n}_{\perp}, \quad \text{on } S_{\rm L}, S_{\rm R}, \tag{16}$$

where $\hat{n}_{\perp}$ is the unit vector normal to the glottal surface. Equation (16) implies that both (structural and flow) sides of the glottal surface are coincident at all times and tractions on both sides balance each other.

The fluid solver is implemented in FLUENT (version 12.0.16, Ansys, Inc., Pennsylvania, USA), the solid solver in ABAQUS (version 6.10, Dassault Systèmes Simulia Corp., Rhode Island, USA) and the coupling between the codes is achieved using MpCCI (version 4.0.1, Scapos AG, Sankt Augustin, Germany).

2.2. Review of Experiments

2.2.1. Rigid Vocal Fold Models

Scherer et al. (2001) considered the flow through a quasi-two-dimensional glottal tract model with rigid VF geometry (defined therein as M5 geometry). In their experiments Scherer et al. (2001) measured airflow pressure distributions on the glottal surface at the mid-coronal section using pressure taps. We focus on

the model considered in Scherer et al. (2001) where the minimum glottal diameter was $d_g = 0.04$ cm, the included glottal angle was 10° (divergent), and the glottis possessed an obliquity of 0°. The TPD was held constant at two levels, 3.00 cm water and 15.0 cm water. The model and TPD cases correspond to the computational model with rigid VFs defined in section 2.1.1.

It is relevant to consider the variations in the included glottal angle and the minimum glottal diameter because such variations are expected when the flexible VFs (section 2.1.2) undergo deformation during FSI. In Li et al. (2006a) the effect of included glottal angle was considered. A series of included glottal angles from −40° (converging) to 40° (diverging) were considered while the minimum glottal diameter was fixed at 0.6 mm and TPD was fixed at 5 cm water. The change in glottal angle was accommodated by modifying the entrance glottal radius. The VF geometry was based on the M5 model but the superior surface was oriented 45° to the axial direction; this modification has been shown to have a negligible effect on the flow pressures (Li et al., 2006b). The flow pressure was not measured on the VF wall, but on the side walls of the channel. The same study showed excellent correspondence between flow pressures measured on the side wall and flow pressure on the VF wall obtained from flow computations on rigid VF models with identical geometry. In the present study the flow pressures measured for the case of included glottal angle equal to −5° (convergent) are considered. In Fulcher et al. (2011) the variation of minimum glottal diameter was considered over a range of TPD. A series of minimum glottal diameters from 0.05 mm to 3.2 mm were considered and TPD was varied from 1–25 cm water. The VF geometry followed the M5 definition and both the included glottal angle and glottal obliquity are set to 0°. Fulcher et al. (2011) analyzed the measured flow pressure profiles and suggested a set of equations (Eqns. 4-6 in that paper) to characterize the flow pressure profile for an arbitrary minimum glottal diameter and TPD. In these equations, entrance and exit loss coefficients appear as parameters. The dependence of these coefficients on TPD was provided in the study. In the present study, these equations are used to predict wall flow pressures for minimum glottal diameter and TPD values corresponding to those attained instantaneous during FSI. Finally, Li et al. (2012) studied the effect of changing the entrance radius over a range of included glottal angles and with minimum glottal diameter fixed at 0.2 mm. The rigid VF shapes considered were based on the M5 geometry. Instead of the TPD, the glottal airflow rate was held fixed at 73.2 cm^3/s. In this paper, measurements obtained by Li et al. (2012) for two different included glottal angles 5° and 10° (both divergent) are considered.

2.2.2. Flexible Vocal Folds

Spencer et al. (2008) considered an experimental set-up that comprised a pair of synthetic rubber models of the VFs, enclosed within a rectangular channel of length 200 mm in the streamwise direction. Constant volume flow rates were maintained in the rectangular channel for 45 minutes to attain periodic vibration states. The downstream end of the rectangular channel coincided with the superior surface of the folds. This allowed for an unobstructed view of the vibrating VFs from the superior aspect, while the flow exited from

the glottis into the open ambient. In contrast, the flow domain in the computational model with flexible VFs (section 2.1.2) has a 20.0 mm long supraglottal tract. The M5 geometry of the synthetic VF models used by Spencer et al. (2008) is identical to that shown in Fig. 2a, except that initially the included glottal angle was 0° and the minimum glottal diameter was $d_g = 0$. Indentation tests with flat cylindrical indenter performed on the synthetic model showed that the constitutive behaviour of the silicone rubber material was linear elastic with negligible viscoelasticity. The Young's modulus deduced from the indentation response was found to be $E = 6.00$ kPa, assuming incompressibility. Therefore the geometry and constitutive properties of the experimental model of Spencer et al. (2008) corresponds to the computational model with flexible VFs. In Spencer et al. (2008) the VFs were excited by imposing an average airflow rate $Q_0 = 406$ cm^3/s at the inlet. Using digital image correlation techniques the inferior–superior and medial–lateral displacement components were measured on the superior-surface along line AB.

2.3. Analysis approach

2.3.1. Rigid Vocal Folds

In the rigid VF experimental configurations considered here (Scherer et al., 2001; Li et al., 2012, 2006a; Fulcher et al., 2011) the flow pressure was measured along curves formed by the intersection of the mid-coronal plane ($x_{\text{ap}} = 0$) with the left and right VF surfaces. Pressure profiles throughout this paper are considered along these curves. The flow pressure profiles on the two VFs are typically non-identical, which is reflected in the asymmetry of the jet downstream (Coanda effect). The side from which the jet detaches further downstream is the flow wall; accordingly, the other side is the non-flow wall. The pressure profiles on both the flow and non-flow walls measured in the M5 experiment (Scherer et al., 2001) are compared to the values of pressure profiles in the present computational model with 2D rigid VFs. The comparison is made for the TPDs considered (3.00 and 15.0 cm of water). For comparison between the computational model data and experimental data identical physical quantities are symbolically distinguished throughout the paper. Unless otherwise stated, quantities with a $\tilde{()}$-accent are computed.

2.3.2. Flexible Vocal Folds

For the purpose of comparing flow pressure on the moving–deforming VF wall, a distance measure referred to as chord length is introduced. Consider the curves formed by the intersection of the left and right VF surfaces and the mid-coronal plane ($x_{\text{ap}} = 0$). The chord length is the distance measured along the curves from the inferior extremity of the VFs ($x_{\text{is}} = -T, x_{\text{ml}} = \pm W/2, x_{\text{ap}} = 0$). Unlike the axial distance measure, chord lengths always increase monotonically along the curves, a feature especially relevant as the VFs deform during vibration.

Airflow pressure obtained from experiments on rigid VF models with varying glottal angles (Fulcher et al., 2011; Li et al., 2012) is compared with airflow pressure computed during the ramp phase. The

comparison is made by considering pressure profiles at the VF mid-coronal section. The measured pressure values are normalized by the experimentally imposed average TPD, whereas the computed pressure values are normalized by the instantaneous TPD during ramp. The imposed average TPD $p^*_{\max}$ in the flexible VF experiment (Spencer et al., 2008) is determined from the average imposed flow-rate Q_0 as

$$p^*_{\max} = aQ_0 + b, \qquad (a, b: \text{ constants}). \tag{17}$$

Here constants a and b are determined from a linear approximation to the relationship between the instantaneous airflow pressure at the inlet p_{in} and the computed instantaneous volume flow rate through the outlet

$$\tilde{Q} \;=\; \int\limits_{x_{\text{is}}=T_{\text{exit}}} \vec{v} \cdot \mathrm{d}\vec{S}. \tag{18}$$

During free vibration, the VFs undergo cyclic motion about a mean deformed state, motivating the decomposition of physical quantities into mean and fluctuation components. The cyclic motion comprises a closing phase, during which the VFs approach each other, and an opening phase, during which the VFs move apart. To compare the experimental measurements and computed values during free-vibration, it is useful to consider only a few representative instants. Therefore, we define that a vibration cycle 'starts' (while the previous cycle 'ends') at the moment the VFs are in the maximum open state. Strictly, the 'maximum open' state is defined as the time instant at which the medial-lateral displacement u_{ml} at $\vec{X}_{\text{SS}}$ is the most negative during a cycle. The 'maximum open' state also marks the beginning of the closing phase. Similarly, the 'maximum closed' VF state corresponds to the most positive value of u_{ml} at $\vec{X}_{\text{SS}}$. The 'maximum closed' state marks the beginning of the opening phase of the cycle.

Airflow pressure is computed at representative instants within the closing phase of a free-vibration cycle. These are compared with those from experiments on rigid VF models with varying glottal angles and varying minimum glottal diameters (Fulcher et al., 2011; Li et al., 2012). The comparison is made by considering pressure profiles at the VF mid-coronal section. The measured pressure values are normalized by the experimentally imposed average TPD, whereas the computed pressure values are normalized by the inlet pressure which remains constant during free-vibration.

The deformed VF shapes during opening and closing phases are similar, but occur in reverse order. Thereby, a mean displacement field is defined as the arithmetic average of the displacements at recorded instants during the opening phase. For the experimental data, the mean inferior–superior and medial–lateral displacements are defined as

$$\langle u_{\text{is}} \rangle = \frac{1}{N} \sum_{k=1}^{N} u_{\text{is}}^{(k)} \qquad \text{and} \qquad \langle u_{\text{ml}} \rangle = \frac{1}{N} \sum_{k=1}^{N} u_{\text{ml}}^{(k)}, \tag{19}$$

where the inferior–superior and medial–lateral components of displacement of the line AB are denoted as $u_{\text{is}}^{(k)}$ and $u_{\text{ml}}^{(k)}$ respectively, and $k = 1 \ldots N$ is any of the N equally spaced time-instants within the opening

phase. For the computational model, consider a vibration cycle with data recorded at N equally spaced time-instants within the opening phase. The mean state is approximated using similar expressions as above

$$\langle \tilde{u}_{\rm is} \rangle = \frac{1}{N} \sum_{k=1}^{N} \tilde{u}_{\rm is}^{(k)} \qquad \text{and} \qquad \langle \tilde{u}_{\rm ml} \rangle = \frac{1}{N} \sum_{k=1}^{N} \tilde{u}_{\rm ml}^{(k)}. \tag{20}$$

In the experiment and in the computation, N is related to the frequency at which data was recorded. The fluctuation amplitude of displacement components were obtained in the experiment as

$$u'_{\rm is,0} = u_{\rm is}^{(k=N)} - \langle u_{\rm is} \rangle \qquad \text{and} \qquad u'_{\rm ml,0} = u_{\rm ml}^{(k=N)} - \langle u_{\rm ml} \rangle, \tag{21}$$

where the condition $k = N$ refers to the maximum open state. Similarly, for the computational model, the fluctuation amplitude of displacement components within a vibration cycle are obtained as

$$\tilde{u}'_{\rm is,0} = \tilde{u}_{\rm is}^{(k=N)} - \langle \tilde{u}_{\rm is} \rangle \qquad \text{and} \qquad \tilde{u}'_{\rm ml,0} = \tilde{u}_{\rm ml}^{(k=N)} - \langle \tilde{u}_{\rm ml} \rangle. \tag{22}$$

Lastly, time variation of the displacement components throughout the cycle is defined as

$$\tilde{f}_{\rm is}(k) = \frac{\tilde{u}_{\rm is}^{k} - \langle \tilde{u}_{\rm is} \rangle}{\tilde{u}'_{\rm is,0}} \qquad \text{and} \qquad \tilde{f}_{\rm ml}(k) = \frac{\tilde{u}_{\rm ml}^{k} - \langle \tilde{u}_{\rm ml} \rangle}{\tilde{u}'_{\rm ml,0}}. \tag{23}$$

The actual displacement field is predicted from normalized computed displacement fields. For example, consider the medial–lateral displacement component. The computed mean displacement field $\langle \tilde{u}_{\rm ml} \rangle$ is normalized by $p_{\rm max}$ to obtain $\langle \tilde{u}_{\rm ml} \rangle / p_{\rm max}$. The mean displacement predicted under experimental conditions is therefore $\langle \tilde{u}_{\rm ml} \rangle (p^*_{\rm max}/p_{\rm max})$. This predicted mean displacement is compared with the measured mean medial–lateral displacement $\langle u_{\rm ml} \rangle$. The computed amplitude of fluctuation displacement $\tilde{u}'_{\rm ml,0}$ is normalized by the local amplitude of fluctuation displacement $\tilde{u}'_{\rm ml,0}(\vec{X}_{\rm SS})$. The amplitude of fluctuation in the medial-lateral displacement is predicted to be $\tilde{u}'_{\rm ml,0}(u'_{\rm ml,0}(\vec{X}_{\rm SS})/\tilde{u}'_{\rm ml,0}(\vec{X}_{\rm SS}))$ under experimental conditions. The corresponding predictions in the inferior–superior direction are $\langle \tilde{u}_{\rm is} \rangle (p^*_{\rm max}/p_{\rm max})$ (mean) and $\tilde{u}'_{\rm is,0}(u'_{\rm is,0}(\vec{X}_{\rm SS})/\tilde{u}'_{\rm is,0}(\vec{X}_{\rm SS}))$ (fluctuation). The spatial correlation between the predicted and measured mean and fluctuation displacement components over line AB is analyzed. Finally, the fluctuation amplitude term multiplied by the time-varying term and added to the mean displacement field gives the total predicted displacement field,

$$u_{\rm ml}^{*(k)} = \langle \tilde{u}_{\rm ml} \rangle \left(\frac{p^*_{\rm max}}{p_{\rm max}} \right) + \tilde{u}'_{\rm ml,0} \left(\frac{u'_{\rm ml,0}(\vec{X}_{\rm SS})}{\tilde{u}'_{\rm ml,0}(\vec{X}_{\rm SS})} \right) \tilde{f}_{\rm ml}(k), \qquad k = 1 \ldots N, \tag{24}$$

which can be readily compared with the experimentally measured medial–lateral displacement $u_{\rm ml}^{(k)}$ over line AB. The corresponding expression for the inferior–superior component is

$$u_{\rm is}^{*(k)} = \langle \tilde{u}_{\rm is} \rangle \left(\frac{p^*_{\rm max}}{p_{\rm max}} \right) + \tilde{u}'_{\rm is,0} \left(\frac{u'_{\rm is,0}(\vec{X}_{\rm SS})}{\tilde{u}'_{\rm is,0}(\vec{X}_{\rm SS})} \right) \tilde{f}_{\rm is}(k), \qquad k = 1 \ldots N, \tag{25}$$

and is compared to the experimentally measured inferior–superior displacement $u_{\rm is}^{(k)}$.

3. Results

3.1. Rigid Vocal Folds

Fig. 3a shows the flow pressure measurements (Scherer et al., 2001) on the left and right VFs as a function of axial location measured on the mid-coronal plane ($x_{\mathrm{ap}} = 0$). Pressure profiles corresponding to different TPD levels within the range 294 to 1470 Pa are plotted. Pressure profiles are characterised by a sharp pressure drop behind the glottal entrance, followed by a recovery region. The imposed TPD is recovered close to the glottal exit. Within the glottis, flow separation at the non-flow wall and attachment to the flow wall is reflected in the higher flow pressures on the non-flow wall compared to corresponding locations on the flow wall. For the bounding cases $p_{\max} = 294$ Pa and 1470 Pa, pressure profiles computed with the rigid model were in good agreement with those from experiment (Fig. 3b). The R^2 correlation was found to be at least 0.954 between corresponding profiles from experiment and computation. The differences between the experimentally measured and computed maximum pressure drop across the glottis are not more than 6.05 %

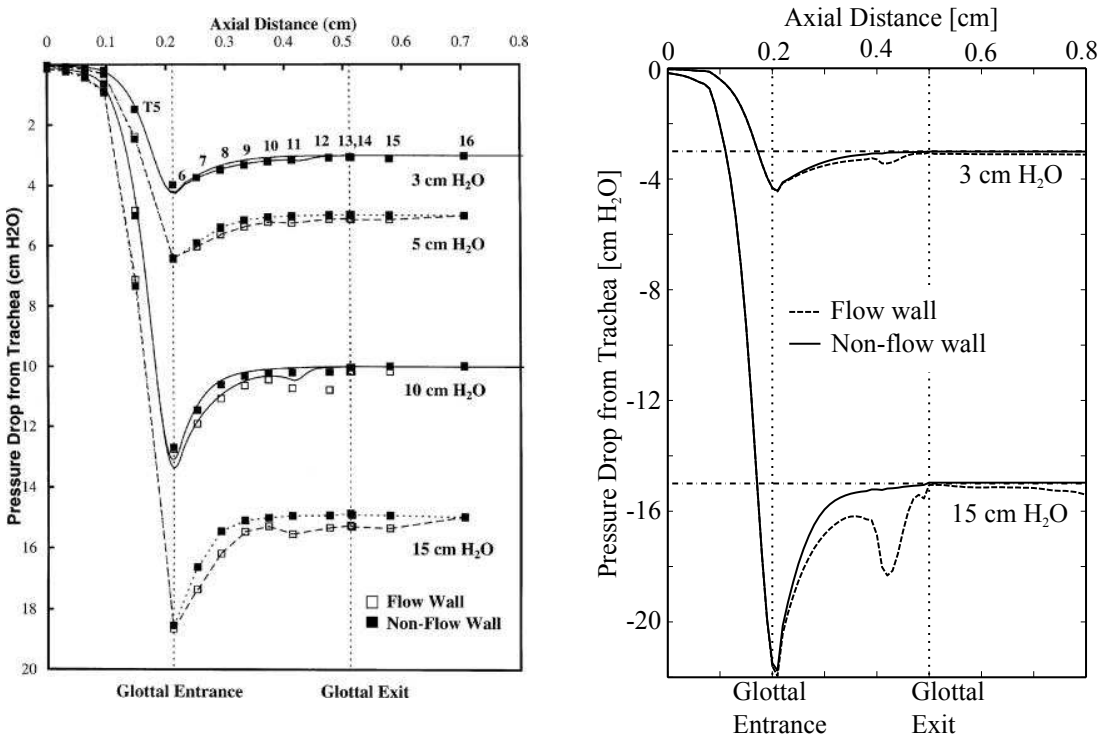

(a) (b)

Figure 3: Intraglottal pressure distribution in absence of FSI: (a) from experiments and (b) from present computations. Fig. 3(a) reprinted with permission from Scherer et al. (2001). Copyright (2001), Acoustic Society of America.

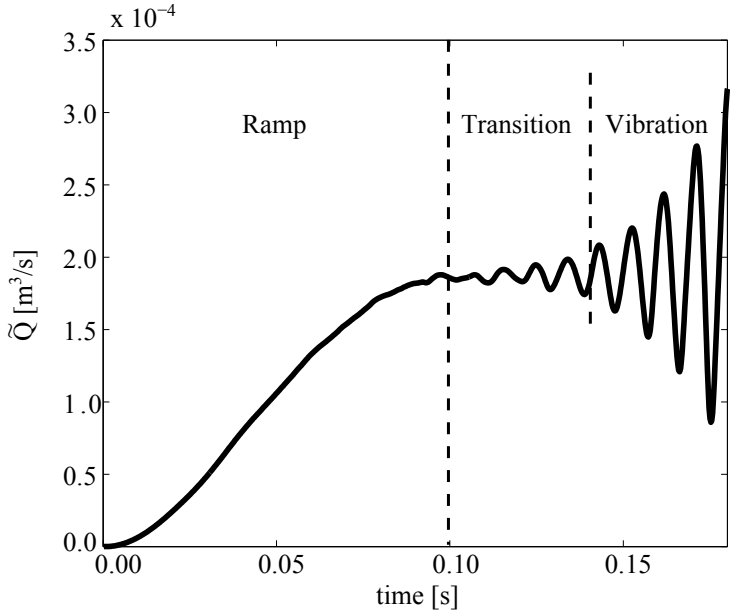

Figure 4: Computed volume flow rate in dependence of time.

for $p_{\max} = 294$ Pa. For $p_{\max} = 1470$ Pa, the differences are within 17.7 %. The location of the secondary pressure minima at the flow wall, for both $p_{\max} = 294$ Pa and 1470 Pa, match well between experiment and present computations (with 0.1 mm of each other). However, the computed pressure drop at secondary pressure minima on the flow wall for the 1470 Pa case is overestimated compared to the measured value.

3.2. Flexible Vocal Folds

3.2.1. Ramp Phase

Fig. 4 shows the computed volume flow rate $\tilde{Q}$ with respect to time. In the ramp phase, the development of flow rate with time indicates that the vibrations are negligible. During the ramp phase, the relation between inlet pressure p_{in} and flow rate was found to be nearly linear ($R^2 = 0.990$) with $a = 1.69$ Pa.s/cm^3 and $b = -85.1$ Pa. Substituting in (17) the equivalent experimental TPD is obtained as $p^*_{\max} = 601$ Pa.

For three instants within the ramp phase of the computational model, $t = 0.0218$ s, 0.0459 s and 0.0784 s, the corresponding instantaneous mid-coronal glottal shapes are shown in Fig. 5a-c. As the TPD increases monotonically during ramp, the included glottal shape becomes increasingly divergent. The normalized flow pressure drop is plotted in dependence of chord length for the three time-instants (Fig. 5d). The results demonstrate that with increase in time the minimum pressure location moves upstream, and the pressure drop through the glottis increases. This behavior compares well with that of the normalized wall pressure profiles obtained in experiments with rigid VFs (Scherer et al., 2010) with respective divergent glottal angles. Note that unlike in the rigid VFs, in the FSI model the independent coordinate (chord length) at material points varies with time, although this variation was less than 3 % throughout the computation.

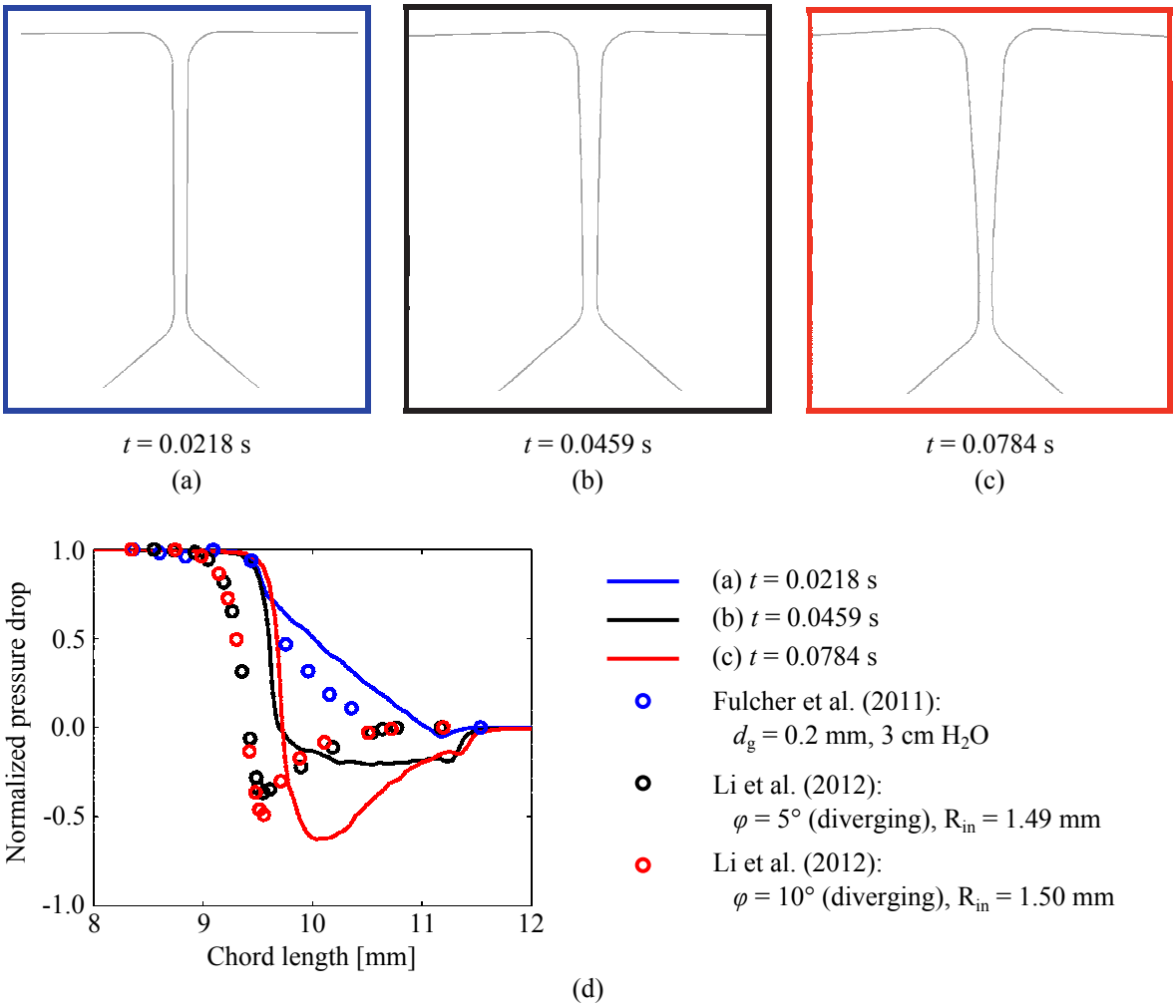

Figure 5: (a)–(c) VF deformed shapes at three different time instants within the ramp phase of the FSI computation. (d) Normalized pressure drops computed on the mid-coronal surface of the left VF wall at the identical instants are plotted in dependence of chord length (solid lines). Normalized pressure drops from experiments (Fulcher et al., 2011; Li et al., 2012) on rigid VFs with different glottal angles are shown with circles.

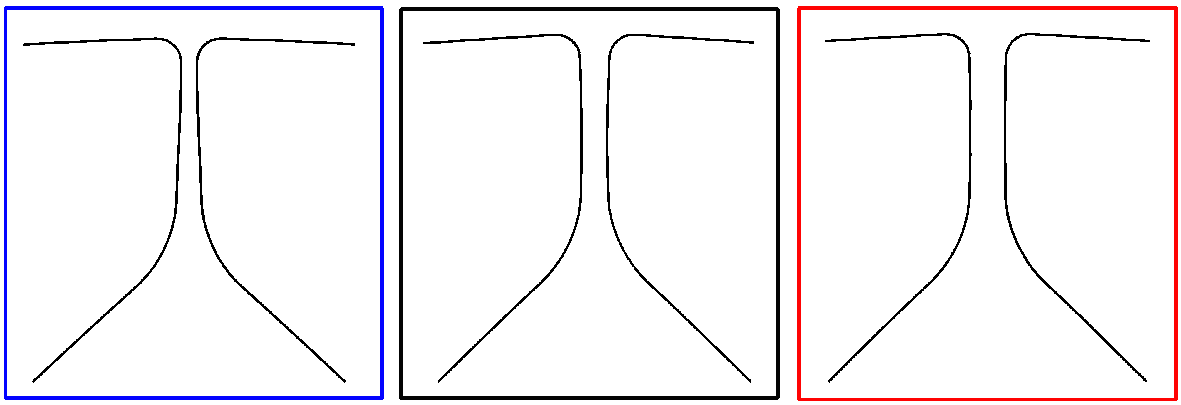

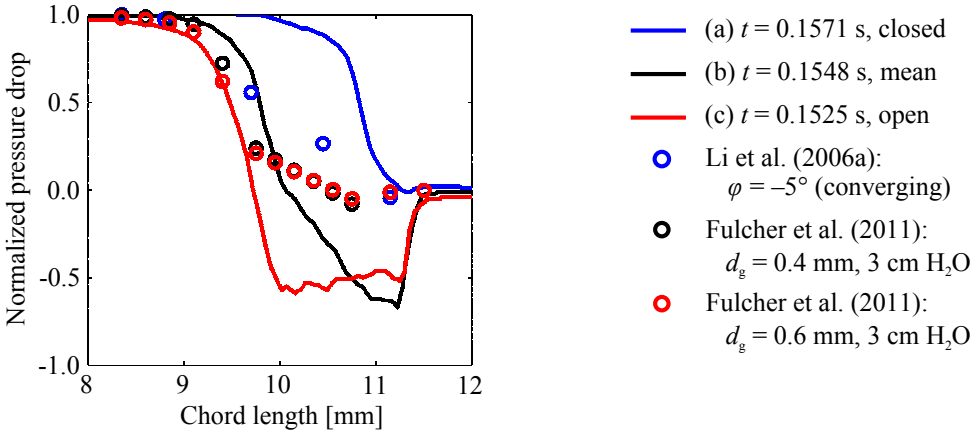

(d)

Figure 6: (a)–(c) VF deformed shapes at instants corresponding to closed, mean and open states within a vibration cycle of the FSI computation. (d) At identical instants and on the mid-coronal surface of the left VF wall, the normalized pressure drops in dependence of chord length are shown by solid lines. Normalized pressure drops obtained from experiments (Li et al., 2006a; Fulcher et al., 2011) on rigid VF models with different included glottal angles and different minimum glottal diameters are shown with circles.

Consider the computed inferior-superior displacements along line AB normalized by the instantaneous TPD, i.e. $\tilde{u}_{\rm is}/p_{\rm in}$, at three instants within the ramp phase, $t = 0.02$, 0.04, 0.06 and 0.08 s. The correlation between the normalized fields was at least $R^2 = 0.999$. The maximum normalized displacement (typically occurring near the mid-coronal plane) differed by at most 11.0 % at the four instants considered.

3.2.2. Well-defined Vibration Phase

In the computational FSI model four consecutive vibration cycles were identified. The cycles start at times $T_1 = 0.1340$ s, $T_2 = 0.1430$ s, $T_3 = 0.1525$ s and $T_4 = 0.1617$ s. The respective cycle time periods are 0.0090 s, 0.0095 s, 0.0092 s and 0.0095 s (mean 0.00930 s, SD 2.63%). The average cycle time period is thus $\tilde{t}_{\rm cycle} = 0.00930$ s (frequency, $\tilde{f} = 108$ Hz) while the experimentally observed values were $t_{\rm cycle} = 0.0112$ s ($f = 89.5$ Hz). Both the experimental and computed values of f are different from the result of linear perturbation analysis conducted *in-vacuo* on the VF structure. The first *in-vacuo* eigenmode of the VFs corresponded to a frequency of 45.7 Hz.

For cycle 3 (starting at T_3 and ending at T_4) the instantaneous mid-coronal glottal shapes corresponding to the instants of maximum open ($t = 0.1525$ s), mean ($t = 0.1548$ s) and maximum closed ($t = 0.1571$ s) are shown in Fig. 6a-c. During each cycle of vibration, the divergence of the VF opening is maximum in the maximum open state, and it is minimum in the maximum closed state. Pressure profiles on the left VF at corresponding instants (Fig. 6d) are compared with those from rigid VF models with different included glottal angles. As the intra-glottal angle decreases (becomes more convergent) during the closing phase, the distribution of flow pressure on the VF wall gets modified. In particular, the increase in convergence causes the minimum pressure location to move upstream. This feature is qualitatively similar to wall pressures measurements from rigid models with glottal angles of increasing convergence.

The inferior–superior displacement $u_{\rm is}$ of the line AB, recorded at $N = 18$ equal time intervals within the opening phase of an experimentally observed vibration cycle are averaged to obtain $\langle u_{\rm is}\rangle$ and shown in Fig. 7. In the computational model, for the cycle starting at T_3 and ending at T_4, the displacement is averaged over $N = 46$ instants at equal intervals of 0.0001 s. The average inferior–superior displacement from the experiment $\langle u_{\rm is}\rangle$ is compared with the predicted displacement $(p^*_{\rm max}/p_{\rm max}) \cdot \langle \tilde{u}_{\rm is}\rangle$ in Fig. 7. Fig. 8a shows the experimentally measured inferior–superior displacements $u_{\rm is}$ of the line AB at each of the 18 time instants of the opening phase. The inferior-superior displacement along line AB predicted at different instants of opening phase using the computed displacements in (25) is shown in Fig. 8b. Fig. 9a shows the medial–lateral displacement $u_{\rm ml}$ of the line AB measured experimentally at the same $N = 18$ instants within the opening phase as considered above. Fig. 9b shows the predicted displacements $u^*_{\rm ml}$ obtained using (24). A quantitative comparison between the figures can be made by considering the average and fluctuation amplitude fields separately. The correlation between the average inferior–superior displacement $\langle u_{\rm is}\rangle$ obtained from the experiment and the predicted displacement $(p^*_{\rm max}/p_{\rm max}) \cdot \langle \tilde{u}_{\rm is}\rangle$ using the computed

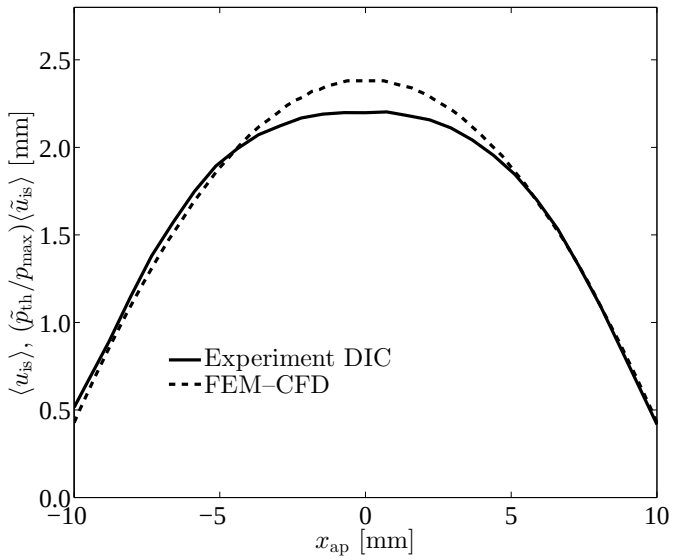

Figure 7: Comparison of cycle-averaged inferior-superior displacement along line AB between experiment and computation. Note that the computed field is scaled to match the flow rate.

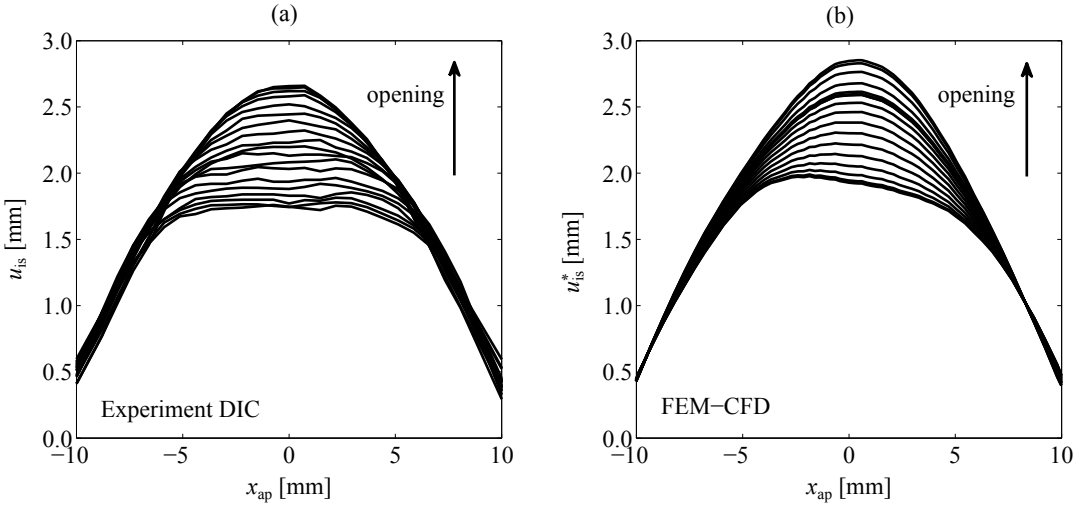

Figure 8: Inferior–superior displacement along line AB. (a) At $N = 18$ instants within an opening cycle measured experimentally. (b) At the same $N = 18$ instants derived from the computed mean and fluctuation fields using (25).

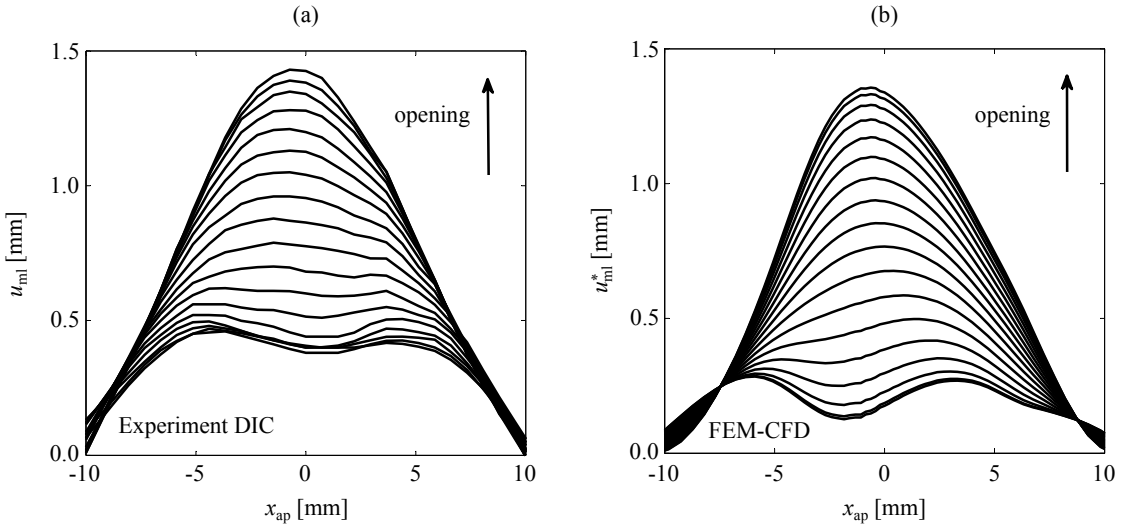

Figure 9: Medial–lateral displacement along line AB. (a) At $N = 18$ instants within an opening cycle measured experimentally. (b) At the same $N = 18$ instants derived from the computed mean and fluctuation fields using (24).

displacements in the cycle starting at T_3 is $R^2 = 0.991$. The percentage difference between $\langle u_{\mathrm{is}} \rangle$ and $(p^*_{\max}/p_{\max}) \cdot \langle \tilde{u}_{\mathrm{is}} \rangle$ at $\vec{X}_{\mathrm{SS}}$ is 8.11 %. The correlation between the inferior–superior displacement fluctuation obtained from computation $\tilde{u}'_{\mathrm{is},0}$ and experimentally observed $u'_{\mathrm{is},0}$ was found to be $R^2 = 0.928$. The correlation between the average medial–lateral displacement $\langle u_{\mathrm{ml}} \rangle$ obtained from the experiment and the predicted displacement $(p^*_{\max}/p_{\max}) \cdot \langle \tilde{u}_{\mathrm{ml}} \rangle$ using the computed displacements in the cycle starting at T_3 is $R^2 = 0.957$. The percentage difference between $\langle u_{\mathrm{ml}} \rangle$ and $(p^*_{\max}/p_{\max}) \cdot \langle \tilde{u}_{\mathrm{ml}} \rangle$ at $\vec{X}_{\mathrm{SS}}$ is 11.0 %. The correlation between $u'_{\mathrm{ml},0}$ and $\tilde{u}'_{\mathrm{ml},0}$ is found to be $R^2 = 0.967$.

4. Discussion

Two-dimensional flow computation is the starting point in the present investigation. Fig. 3 shows that the pressure drop and the extent of recovery region, as computed by the flow solver, matches well with the experimental observations. The agreement is better for $p_{\max} = 294$ Pa, which gives confidence in the FSI computations conducted at a TPD of 300 Pa. The self-similarity in the flow pressure over the VF walls for $p_{\max} = 294$ and 1470 Pa suggest that the pressure profile as computed by the flow solver at $p_{\max} = 294$ Pa can be scaled up by the TPD ratio to obtain the wall pressure for any intermediate case.

For the 3D computational model with flexible VFs, the form of ramp-up pressure specified in (6) is smooth up to the second-derivative. This choice has been found to reduce impulsive forcing during the ramp phase, as confirmed by the absence of airflow fluctuations in this phase (Fig. 4). Therefore the VF vibrations studied here are entirely self-sustained and not externally forced. Further Fig. 5 demonstrates

that during the ramp phase the gradual opening of the glottis causes the flow pressure profile on the VF wall to undergo qualitative changes which are similar to those measured on rigid VF geometries with varying glottal angles. In particular the normalized maximum pressure drop agrees well, as does the rate of pressure drop at the region upstream of the glottal entrance. Quantitative differences between experiment and computational model predictions can be traced to multiple sources (Table 3) which are either differences in glottal geometry or differences in TPD. For example stretching of the VFs in the superior-direction during ramp perhaps directly causes the FSI-associated curves to shift in the superior-direction in Fig. 5d. In the glottal region the chord length of a material point can increase by as much as 0.5 mm due to stretching, and the shift in Fig. 5d is of the same order of magnitude. Note that such a shift would be observed even if axial distance was chosen as the independent coordinate. However, the advantage in plotting pressure profiles in dependence of chord length is that the profiles remain single-valued under VF deformation.

Table 3: Computed VF geometry parameters (definitions in Fig. 10) and TPD values at instants considered within ramp phase (Fig. 5). In parenthesis values are provided for the same parameter but from closely approximating rigid VF replica experiments available from literature. For the computational VF FSI model, entrance and exit radii are assumed unchanged with respect to pre-phonatory state. Rigid VF cases that deviate by more than 5% from the FSI cases are given in bold.

Parameter	$t = 0.0218$ s	$t = 0.0459$ s	$t = 0.0784$ s
d_g [mm]	0.2(0.2)	0.2(0.2)	0.2(0.2)
φ [°]	0(0)	4(**5**)	7(**10**)
ψ [°]	50(50)	49(50)	49(50)
β [°]	0(0)	1.5(0)	3.5(0)
R_{in} [mm]	1.5(1.5)	1.5(1.49)	1.5(1.5)
R_{out} [mm]	0.987(0.987)	0.987(**1.08**)	0.987(**1.08**)
TPD [Pa]	36.6(**294**)	132(**608**)	264(**559**)

The computed frequency of VF vibration $\tilde{f} = 108$ Hz did not correspond to the computed frequency of the first *in-vacuo* mode. This is not surprising since the frequency of the coupled system, comprising two very different domains, cannot be expected to vibrate with the frequency of either domains. The experimentally observed frequency $f = 89.5$ Hz, though somewhat smaller, was still much different from the *in-vacuo* frequency. Linear perturbation analysis of models of the coupled FSI system (Zhang et al., 2007; Zhang, 2009) strongly support the distinction between *in-vacuo* and FSI frequencies.

The changes in glottal angle and minimum glottal diameter during free-vibration caused the distribution of flow pressure on the VF wall to vary (Fig. 6). Qualitative agreement was demonstrated between this variation and the differences between flow pressure measured on rigid VFs with varying glottal angles and

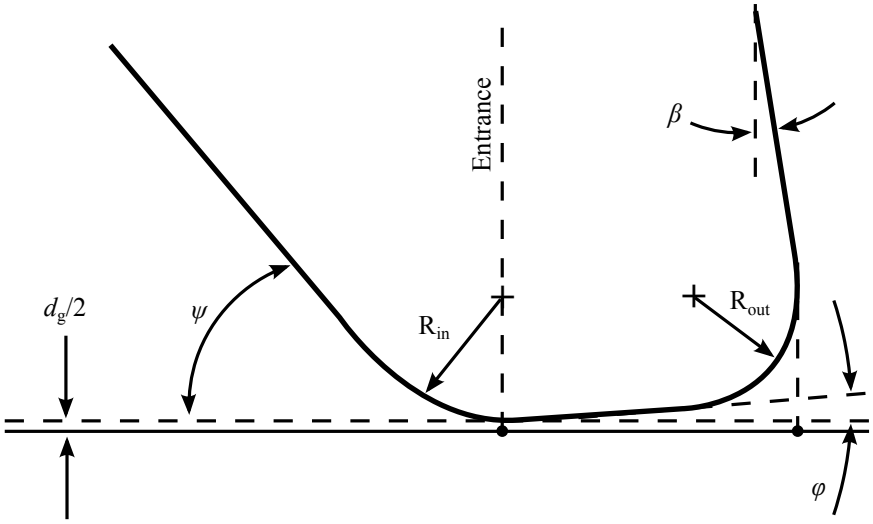

Figure 10: Definition of VF geometry parameters.

varying minimum glottal diameters. The result can be considered in general support of the flow solver, especially during FSI. The present results are a first instance where a comparison between rigid and flexible models has been made. There are no experimental measurements of flow-pressure on the wall of a self-oscillating deformable VF. Thus a direct quantitative validation of the computed flow pressures was not possible. In fact, the computed wall flow pressures at different instants of the vibration cycle did not present a quantitative match with the flow pressure measured on rigid VFs. This is expected because the intra-glottal angles and minimum glottal diameters attained during vibration were not identical to those in the rigid VF models considered (Table 4). Differences between the rigid and FSI model pressure profiles both in Figs. 5 and 6 are also attributable to deviations from quasisteady flow. Deviations from quasisteady flow are expectedly to be higher in the well-defined vibration phase compared to the ramp phase. These reflect the larger deviations in Fig. 6 compared to those in Fig. 5.

The self-similarity of normalized displacement of line AB computed during the ramp phase suggests that normalized displacement field can be used even for higher TPDs that are close to experimental values. Thereby, a normalization procedure is used to predict the mean displacement field in Fig. 7 which matches with the experimental measurement. Similar to the rigid VF pressure profiles in Fig. 3 the flow is expected to attach asymmetrically to either the left of right VF during ramp and vibration, resulting in asymmetric wall pressure distribution. However, using a two-mass model for VF dynamics, Erath et al. (2011a,b) have shown that the asymmetry in flow pressures on the flow and non-flow walls do not cause significant asymmetry in VF deformation if the tissue properties are symmetric, which is the case in the current investigation. Thereby, both absolute and normalized computed displacements obtained on the left VF can be taken to be representative of either VF.

Table 4: Computed VF geometry parameters (definitions in Fig. 10) and TPD values at instants considered during VF vibration (Fig. 6). In parenthesis values are provided for the same parameter but from closely approximating rigid VF replica experiments available from literature. For the computational VF FSI model, entrance and exit radii are assumed unchanged with respect to pre-phonatory state. Rigid VF cases that deviate by more than 5% from the FSI cases are given in bold.

Parameter	$t = 0.1571$ s	$t = 0.1548$ s	$t = 0.1525$ s
d_{g} [mm]	0.3(**0.6**)	0.4(0.4)	0.6(0.6)
φ [°]	-4(**-5**)	1(**0**)	0(0)
ψ [°]	46(44)	46(**50**)	47(**50**)
β [°]	2.5(**-45**)	3.5(**0**)	3.5(**0**)
R_{in} [mm]	1.5(**1.8**)	1.5(1.5)	1.5(1.5)
R_{out} [mm]	0.987(**0.7**)	0.987(0.987)	0.987(0.987)
TPD [Pa]	300(**490**)	300(294)	300(294)

Fig. 8 demonstrates that the computed spatial distribution of total (mean and fluctuation) inferior–superior displacement along AB is in agreement between experiment. The very small fluctuation near the anterior and posterior ends, as observed in the experiment, is predicted from the computed fields. This three-dimensional characteristic is not obvious and indicates a complex interplay between the flow and the structure. The agreement between computation and experiment was found to extend to the spatial distribution of medial–lateral displacement as well (Fig. 9). The correspondence between observed and computed medial–lateral displacement suggests that computed stress fields (in particular the fluctuation component) should be normalized by the local fluctuation displacement components $\{u'_{\mathrm{is},0}, u'_{\mathrm{ml},0}\}$ measured at $\vec{X}_{\mathrm{SS}}$.

The validation of the normalization strategy combined with linear superposition is important because the FE solver allowed fully non-linear deformations. In a recent paper (Bhattacharya and Siegmund, in press), the computational FSI modelling framework presented here was employed to investigate the state of stress in the VFs when phonating at two different hydration states. In both states, the VF strains were small enough so that non-linear contributions could be neglected. Further, in that study, the stresses developed within the VFs showed that mean and fluctuation components of VF deformation play different roles in distributing interstitial fluid in the VF tissue. Thus the separation of displacements into mean and fluctuation components provides physical insight into stress analysis. An equally important consequence on linear superposition is the possibility of predicting VF displacement over a range of TPD values using a single computation. This possibility was in fact validated in this paper through the formalism of equations (19)–(25) where computed displacements obtained at a particular flow rate were used to predict displacements

in an experiment conducted at a different flow rate. The ability to predict physically relevant deformations and stresses depends on the ability to measure the average TPD and the components of displacement at a location on the superior surface. Both measurements are readily obtained through well-established procedures (Holmberg et al., 1988; Wittenberg et al., 2000; Spencer et al., 2008; George et al., 2008; Rieves et al., 2009; Chen, 2009).

4.1. Limitations of the computational model

The time-integration scheme in the rigid VF flow solver is first-order implicit, which is lower-order (in discretization) compared to other numerical formulations (Scherer et al., 2001, 2010; Suh and Frankel, 2007). The first-order scheme is the only possible option in the computational FSI model because of limitations on the communication between the flow and structural solvers in the 'segregated' implementation presented here. Therefore the computational model with rigid VF employs a first-order scheme to retain correspondence with the computational model with flexible VFs. Even with the lower-order scheme, the present rigid VF model predicts the wall pressure reasonably well.

Compared to the experimental model with flexible VFs (Spencer et al., 2008), three geometric alterations were incorporated in the computational model. Firstly, the VFs were initially separated by a minimum glottal diameter d_g which was non-zero. Secondly, the glottal geometry was modified to have a slightly convergent (2°) shape. These two changes ensured that the separation between the opposing folds did not become zero at any location, a requirement imposed by the computational fluid dynamics solver (FLUENT). Thirdly, unlike the experimental model of Spencer et al. (2008) where the flow exits into the ambient, the supraglottal tract in the computational model was modified to represent a more realistic geometry. The geometric differences between the computational model and the experimental model presented in Spencer et al. (2008) are assumed to have negligible effect on the determination of flow pressure on the VFs and in the consequent VF deformation characteristics.

The models in Scherer et al. (2010) had an anterior–posterior variation of the medial surface that was symmetric about the mid-coronal plane, unlike the 3D computational model with flexible VFs considered in this paper which was extruded in the anterior–posterior direction. However, since only the mid-coronal (symmetry) plane is considered for comparison of wall pressures between the present computational model and the experimental models of Scherer et al. (2010), the difference in geometry is not expected to be relevant. Additionally, it was observed in Scherer et al. (2010) that the anterior–posterior variation in wall pressure profiles near the mid-coronal plane was in fact negligible.

Several researchers (Tallec and Mouro, 2001; Zhang and Hisada, 2001, 2004; Causin et al., 2005; Förster et al., 2007; van Brummelen and Geuzaine, 2010) have noted that for a segregated computational FSI problem with an incompressible fluid, the solution will always become unstable after a finite number of increments. Indeed, the flexible VF computational model demonstrated numerical instability with time (Fig. 4). This

compares with the experimental model, which for a fixed TPD vibrated with a nearly constant amplitude of vibration. The numerical instability poses two limitations on the present model. Firstly, the continuously increasing computed vibration amplitude is difficult to compare with a fixed measured vibration amplitude. This limitation is overcome by introducing the normalization methodology which was extensively validated. The second limitation is that it is difficult to distinguish the physical instability related to phonation onset behavior from the numerical instability in the current model. However, this does not limit the determination of displacements in a vibrating VF excited at conditions beyond onset, which was the objective of the present study.

The above mentioned instability effect is known to be dependent on domain geometry (Förster et al., 2007). Consequently, compared to the problem of VF FSI, a much reduced unstable behavior is found (Fraunhofer SCAI, 2008) in the case of a standard FSI benchmark problem (Turek and Hron, 2006; Breuer et al., 2012) where the dynamics is induced by vortices in an open flow vortex and determined strongly by structural slenderness. The dynamics in VF FSI in contrast depends on the variation in glottal gap (i.e. displacement of the bulk VF tissue) and the variation in streamwise pressure gradients in the confined glottal flow domain (van den Berg, 1958; Titze, 2006). Due to these differences it is important to validate the present segregated coupling model specifically for VF FSI although this methodology has been validated for problems involving the interaction of vortices with slender structures (Gomes et al., 2011; Bina et al., 2013).

A discussion of the incompressible, laminar flow prescription, employed within the computational FSI model presented herein, is also relevant. The Boussinesq approximation holds for the flow of air through the glottal tract, since Mach numbers typical of phonation are sufficiently small (Scherer et al., 2010). Thereby, assumption of flow incompressibility, and ignoring the effects of acoustics on the deformation of the VF are justified. On the other hand it can be argued that the computed laminar flow solution is not sufficiently accurate to draw inferences regarding the dynamics of the glottal jet. Indeed previous studies (Alipour and Scherer, 2006) indicate that the glottal jet demonstrates turbulent characteristics. A significant difference between turbulent and laminar flow at the VF wall is the wall shear force, or drag, which in the case of turbulent flow is expected to be much larger compared to laminar flow. However, as the tangential drag on the VF results in a much smaller energy transfer to the VFs compared to the normal flow pressure (Thomson et al., 2005) the error in computed shear forces in determining the VF deformation and VF stresses can be neglected. In fact, inviscid flow models (Decker and Thomson, 2007; Sváček and Horáček, 2012) perform satisfactorily in predicting vibration frequency, pressure along the VF wall, and vibration amplitudes, while expectedly giving unsatisfactory results for flow separation characteristics and glottal air flow rate. Finally, studies conducted on rigid VFs (Scherer et al., 2010) indicate that the flow pressures on the glottal surface are well predicted by a laminar flow model. Thus, with respect to determining VF deformation due to interaction with the flow, the laminar flow model employed here is justified.

In (24) and (25) the vibration component was represented as the product of a single spatially-varying

function and a single time-varying (t_{cycle}-periodic) function. The accuracy of predicting the corresponding experimentally recorded displacements was found to be significantly high. However, it is possible that the accuracy would be lowered if the VF tissue constitutive behavior is made physiologically more accurate (see section 4.2 below) leading to more complex vibration patterns. In such cases, vibration characteristics can perhaps be better predicted by following the empirical eigenfunction extraction approach (Berry et al., 1994; Liu et al., 2002; Döllinger et al., 2005; Berry et al., 2006). The linear superposition principle introduced here can readily be applied in conjunction with the empirical eigenfunction extraction approach. For example, let $\langle\tilde{u}_{\text{ml}}\rangle$ and $\tilde{u}'_{\text{ml},j0}$ be respectively the mean and j-th empirical eigenfunction of the medial-lateral displacement extracted following a computation. Then the medial-lateral displacement in the experiment can be predicted as a weighted sum of the first M empirical eigenfunctions,

$$u^{*(k)}_{\text{ml}} = \langle\tilde{u}_{\text{ml}}\rangle \left(\frac{p^*_{\max}}{p_{\max}}\right) + \sum_{j}^{M} \tilde{u}'_{\text{ml},j0} \left(\frac{u'_{\text{ml},j0}(\vec{X}_{\text{SS}})}{\tilde{u}'_{\text{ml},j0}(\vec{X}_{\text{SS}})}\right) \tilde{f}_{\text{ml},j}(k), \qquad k = 1 \ldots N \tag{26}$$

where $\tilde{f}_{\text{ml},j}(k)$ is the j-th temporal eigenfunction associated with $\tilde{u}'_{\text{ml},j0}$, $u'_{\text{ml},j0}$ is the j-th empirical eigenfunction extracted from the experimental results, and M is the number of eigenfunctions that should be included to obtained a desired level of accuracy. It must be noted that even for three-dimensional vocal folds (excised folds or replicas, with or without highly non-linear events e.g. collision) VF vibration can be satisfactorily (up to 75% or more) represented by the first eigenfunction and up to at least 95% by including the first three eigenfunctions (Berry et al., 1994; Döllinger et al., 2005; Berry et al., 2006; Zhang et al., 2007). Hence the use of the empirical eigenfunction approach is expected to yield substantial added benefit for vibration patterns significantly more complex than the ones presently found.

4.2. Limitations of the flexible VF physical replica

The present paper focused on developing a computational model to simulate the vibration of a physical replica of the VFs. A physical replica incorporates some important simplifications in modeling the physiological VF tissue. The influence of these simplifications on the results presented in this paper is discussed in the following.

The stress–strain relationship in physiological VFs is typically hyperelastic (Kelleher et al., 2013a). In contrast the constitutive behavior of the physical replica and the computation model used here is linear elastic. The effect of non-linearity is expected to be significant if the VF strain varies over a sufficiently large range during vibration. For a small range of strain variation, the stress–strain behavior can be effectively linearized around a representative strain value falling within that (small) range. Note that during phonation, the total strain in the VF tissue includes a (typically large) pre-phonatory strain (related to posturing) in addition to that due to average and fluctuation displacements accounted for in this paper. The effect of pre-phonatory strain is twofold: increase in the tangent elastic modulus of VF tissue and alteration

of the geometry of the VFs. Both these changes can be incorporated into the physical replica and the computational model, and do not limit the study here. Thus the effect of non-linear VF tissue behavior limits the present results only if the variation in total strain less the pre-phonatory strain is sufficiently high. Experimental evidence for this condition however is inconclusive. Yet, in case the variation in post-phonatory strain is indeed sufficiently large, the VF tissue stress–strain behavior needs to be characterized accurately, and incorporated both in the physical replica and in the computational model. Moreover, in such a case deviations from linearity, used here to arrive at (24) and (25), will be significant. Hence in order to validate a computational model with hyperelastic VF tissue over a large range of strain, it is necessary to conduct numerical simulations for multiple TPD values.

A physiological VF also has a layered structure (Hirano, 1977; Hirano et al., 1981; Hirano and Kakita, 1985), whereas the flexible VF models defined in this paper are homogeneous. The layered structure has been shown to lead to unique vibration characteristics such as mucosal wave propagation that are representative of voiced speech (Milutinović et al., 1998; Zhang et al., 2009; Sato et al., 2012). Two-layer physical and computational models have been used in the literature (Drechsel and Thomson, 2008; Riede et al., 2008; Mendelsohn and Zhang, 2011). Although not attempted here, the linear superposition method used in the present study can be applied to validate the use of computational models with a layered VF description over a range of TPD.

Another feature not captured in the present paper is the anisotropy of VF tissue (Hirano et al., 1982; Ishii et al., 1996; Miri et al., 2012; Kelleher et al., 2013b). Recent studies have investigated physical VF replicas with anisotropy (Zhang and Xuan, 2013). Anisotropic behavior of VF tissue has been considered in computational models of VF FSI (Alipour et al., 2000; Tao and Jiang, 2007; Zheng et al., 2011). Although the validation method used here can be applied in the case of an anisotropic VF as well, this was not an objective of the present validation study.

5. Conclusions

This study validated a methodology of prediction of VF displacements during self-sustained vibration using a computational model of FSI. The methodology presented depends on decomposing the VF displacement field into a time-invariant mean and a periodic fluctuation. The mean displacement when normalized by the TPD is found to match between computation and experiment. The computed fluctuation displacement was found to match with the experimentally measured values, when normalized by the fluctuation displacement amplitude at a superior-surface location. The correspondence between computed and measured displacements (both medial–lateral and inferior–superior components) extends over a relevant region on the VF superior surface.

An appealing consequence of the self-similarity of the computed normalized displacements is that these

can be used to determine physical displacements over a range of external conditions. If a VF computational model is accurately constructed to resemble a subject-specific VF, a single computation at an arbitrary TPD can be conducted to obtain normalized mean and fluctuation displacement fields. Corresponding normalized mean and fluctuation stress fields in the VF interior can be determined, up to the accuracy to which constitutive properties of the subject-specific VF tissue are known. Thereby, the state of stress during a voice exercise performed in the clinic can be predicted by scaling the computed normalized stresses by measurements of TPD and displacements at a superior-surface location obtained during the voice exercise.

The presented validation study supports the notion that the computed stresses in the VF interior reasonably predict those in the experimental model. Validation of the prediction of VF stresses is critical before one can employ computational models for the analysis of stress-dependent processes such as VF collision, hydration or scarring. Considering the numerous challenges – three-dimensionality, unsteady dynamics, multi-physics domains – the correspondence between the experimental and computational results presented here are very encouraging. The inferred characteristics of systemic hydration during vibration are expected to provide exciting biomechanical insights. An attractive future course of research is the validation of collision-induced pressures on the VF surface. This is required in order to include all the relevant external tractions on the VF tissue during typical phonation. Validation of collision-induced tractions will however need a contact model to be included in the computational framework (Bhattacharya and Siegmund, in press), as well as extracting impact pressures in an experimental set-up.

Acknowledgement

This work was funded by NIDCD Grant 5R01DC008290-04.

References

Alipour, F., Berry, D.A., Titze, I.R., 2000. A finite-element model of vocal-fold vibration. Journal of the Acoustical Society of America 108, 3003–3012.

Alipour, F., Scherer, R.C., 2004. Flow separation in a computational oscillating vocal fold model. Journal of the Acoustical Society of America 116, 1710–1719.

Alipour, F., Scherer, R.C., 2006. Characterizing glottal jet turbulence. Journal of the Acoustical Society of America 119, 1063–1073.

van den Berg, J., 1958. Myoelastic-aerodynamic theory of voice production. Journal of Speech and Hearing Research 1, 227–244.

Berry, D.A., Herzel, H., Titze, I.R., Krischer, K., 1994. Interpretation of biomechanical simulations of normal and chaotic vocal fold oscillations with empirical eigenfunctions. Journal of the Acoustical Society of America 95, 3595–3604.

Berry, D.A., Zhang, Z., Neubauer, J., 2006. Mechanisms of irregular vibration in a physical model of the vocal folds. Journal of the Acoustical Society of America 120, EL36–EL42.

Bhattacharya, P., Siegmund, T., in press. A computational study of systemic hydration in vocal fold collision. Computer Methods in Biomechanics and Biomedical Engineering .

Bina, J., Oatesa, W.S., Hussaini, M.Y., 2013. Fluid-structure interactions of photo-responsive polymer cantilevers. Journal of Fluids and Structures 37, 34–61.

Breuer, M., Nayer, G.D., Münsch, M., Gallinder, T., Wüchner, R., 2012. Fluid-structure interaction using a partitioned semi-implicit predictor-corrector coupling scheme for the application of large-eddy simulation. Journal of Fluids and Structures 29, 107–130.

van Brummelen, E.H., Geuzaine, P., 2010. Fundamentals of Fluid-Structure Interaction. John Wiley & Sons, Ltd.

Causin, P., Gerbeau, J., Nobile, F., 2005. Added-mass effect in the design of partitioned algorithms for fluid-structure problems. Computer Methods in Applied Mechanics and Engineering 194, 4506–4527.

Chan, R.W., Tayama, N., 2002. Biomechanical effects of hydration in vocal fold tissues. Otolaryngology – Head and Neck Surgery 126, 528–537.

Chen, L.J., 2009. Investigations of mechanical stresses within human vocal folds during phonation. Ph.D. thesis. Purdue University.

Decker, G.Z., Thomson, S.L., 2007. Computational simulations of vocal fold vibration: Bernoulli versus Navier-Stokes. Journal of Voice 21, 273–284.

Döllinger, M., Tayama, N., Berry, D.A., 2005. Empirical eigenfunctions and medial surface dynamics of a human vocal fold. Methods of Information in Medicine 44, 384–391.

Drechsel, J.S., Thomson, S.L., 2008. Influence of supraglottal structures on the glottal jet exiting a two-layer synthetic, self-oscillating vocal fold model. Journal of the Acoustical Society of America 123, 4434–4445.

Erath, B.D., Peterson, S.D., Zanartu, M., Wodicka, G.R., Plesniak, M.W., 2011a. A theoretical model of the pressure distributions arising from asymmetric intraglottal flows applied to a two-mass model of the vocal folds. Journal of the Acoustical Society of America 130, 389–403.

Erath, B.D., Zanartu, M., Peterson, S.D., Plesniak, M.W., 2011b. Nonlinear vocal fold dynamics resulting from asymmetric fluid loading on a two-mass model of speech. Chaos 21, 033113.

Förster, C., Wall, W.A., Ramm, E., 2007. Artificial added mass instabilities in sequential staggered coupling of nonlinear structures and incompressible viscous flows. Computer Methods in Applied Mechanics and Engineering 196, 1278–1293.

Fraunhofer SCAI, 2008. MpCCI 3.0.6-21 documentation. Germany.

Fulcher, L.P., Scherer, R.C., Powell, T., 2011. Pressure distributions in a static physical model of the uniform glottis: Entrance and exit coefficients. Journal of the Acoustical Society of America 129, 1548–1553.

Fulcher, L.P., Scherer, R.C., Witt, K.J.D., Thapa, P., Bo, Y., Kucinschi, B.R., 2010. Pressure distributions in a static physical model of the hemilarynx: Measurements and computations. Journal of Voice 24, 2–20.

George, N.A., de Mul, F.F.M., Qiu, Q., Rakhorst, G., Schutte, H.K., 2008. Depth-kymography: high-speed calibrated 3D imaging of human vocal fold vibration dynamics. Physics in Medicine and Biology 53, 2667–2675.

Gomes, J.P., Yigit, S., Lienhart, H., Schäfer, M., 2011. Experimental and numerical study on a laminar fluid-structure interaction reference test case. Journal of Fluids and Structures 27, 43–61.

Guo, C., Scherer, R.C., 1993. Finite-element simulation of glottal flow and pressure. Journal of the Acoustical Society of America 94, 688–700.

Hirano, M., 1977. Structure and vibratory behavior of the vocal folds, in: Sawashima, M., Cooper, F.M. (Eds.), Dynamic aspects of speech production. University of Tokyo Press.

Hirano, M., Kakita, Y., 1985. Cover-body theory of vocal fold vibration, in: Daniloff, R.G. (Ed.), Speech Science: Recent Advances. College Hill Press, San Diego, pp. 1–46.

Hirano, M., Kakita, Y., Ohmaru, K., Kurita, S., 1982. Structure and mechanical properties of the vocal fold, in: Lass, N. (Ed.), Speech and language: advances in basic research and practice. Academic Press, New York. volume 7, pp. 271–297.

Hirano, M., Kurita, S., Nakashima, T., 1981. The structure of the vocal folds, in: Stevens, K.N., Hirano, M. (Eds.), Vocal fold

physiology. University of Tokyo Press, pp. 33–41.

Holmberg, E.B., Hillman, R.E., Perkell, J.S., 1988. Glottal airflow and transglottal air pressure measurements for male and female speakers in soft, normal, and loud voice. Journal of the Acoustical Society of America 84, 511–529.

Ishii, K., Zhai, W., Akita, M., Hirose, H., 1996. Ultrastructure of the lamina propria of the human vocal fold. Acta Oto-laryngolica 116, 778–782.

Kelleher, J.E., Siegmund, T., Du, M., Naseri, E., Chan, R.W., 2013a. The anisotropic hyperelastic biomechanical response of the vocal ligament and implications for frequency regulation: a case study. Journal of the Acoustical Society of America 133, 1625–1636.

Kelleher, J.E., Siegmund, T., Du, M., Naseri, E., Chan, R.W., 2013b. Empirical measurements of biomechanical anisotropy of the human vocal fold lamina propria. Biomechanics and Modeling in Mechanobiology 12, 555–567.

Leydon, C., Sivasankar, M., Falciglia, D.L., Atkins, C., Fisher, K.V., 2009. Vocal fold surface hydration: A review. Journal of Voice 23, 658–665.

Li, S., Scherer, R.C., Wan, M.X., Wang, S.P., 2012. The effect of entrance radii on intraglottal pressure distributions in the divergent glottis. Journal of the Acoustical Society of America 131, 1371–1377.

Li, S., Scherer, R.C., Wan, M.X., Wang, S.P., Wu, H.H., 2006a. The effect of glottal angle on intraglottal pressure. Journal of the Acoustical Society of America 119, 539–548.

Li, S., Scherer, R.C., Wan, M.X., Wang, S.P., Wu, H.H., 2006b. Numerical study of the effects of inferior and superior vocal fold surface angles on vocal fold pressure distributions. Journal of the Acoustical Society of America 119, 3003–3010.

Liu, L., Galatsanos, N.P., Bless, D., 2002. Eigenfolds: a new approach for analysis of vibrating vocal folds, in: Proceedings of the IEEE International Symposium on Biomedical Imaging, 2002, pp. 589–592.

Luo, H., Mittal, R., Bielamowicz, S., 2009. Analysis of flow-structure interation in the larynx during phonation using an immersed boundary method. Journal of the Acoustical Society of America 126, 816–824.

Luo, H., Mittal, R., Zheng, X., Bielamowicz, S.A., Walsh, R.J., Hahn, J.K., 2008. An immersed-boundary method for flow-structure interation in biological systems with application to phonation. Journal of Computational Physics 227, 9303–9332.

McGowan, R.S., 1993. The quasisteady approximation in speech production. Journal of the Acoustical Society of America 94, 3011–3013.

Mendelsohn, A.H., Zhang, Z., 2011. Phonation threshold pressure and onset frequency in a two-layer physical model of the vocal folds. Journal of the Acoustical Society of America 130, 2961–2968.

Milutinović, Z., Polić, D., Milenković, S., Sretenović, V., 1998. Spatial arrangement of the structural elements of vocal fold layers: an adjustment to the vibration process. Journal of Voice 12, 17–20.

Miri, A.K., Mongrain, R., Chen, L.X., Mongeau, L., 2012. Quantitative assessment of the anisotropy of vocal fold tissue using shear rheometry and traction testing. Journal of Biomechanics 45, 2943–2946.

Mittal, R., Erath, B.D., Plesniak, M.W., 2013. Fluid dynamics of human phonation and speech. Annual Review of Fluid Mechanics 45, 437–467.

Mittal, R., Zheng, X., Bhardwaj, R., Seo, J.H., Xue, Q., Bielamowicz, S., 2011. Toward a simulation-based tool for the treatment of vocal fold paralysis. Frontiers in Physiology 2, 19.

de Oliveira Rosa, M., Pereira, J.C., Grellet, M., Alwan, A., 2003. A contribution to simulating a three-dimensional larynx model using the finite-element model. Journal of the Acoustical Society of America 114, 2893–2905.

Riede, T., Tokuda, I.T., Munger, J.B., Thomson, S.L., 2008. Mammalian laryngseal air sacs add variability to the vocal tract impedance: Physical and computational modeling. Journal of the Acoustical Society of America 124, 634–647.

Rieves, A.L., Regner, M.F., Jiang, J.J., 2009. Phonation threshold pressure estimation using electroglottography in an airflow redirection system. The Laryngoscope 119, 2378–2383.

Sato, K., Umeno, H., Nakashima, T., Nonaka, S., Harabuchi, Y., 2012. Histopathologic investigations of the unphonated human

child vocal fold mucosa. Journal of Voice 26, 37–43.

Scherer, R.C., Shinwari, D., DeWitt, K.J., Zhang, C., Kucinschi, B.R., Afjeh, A.A., 2001. Intraglottal pressure profiles for a symmetric and oblique glottis with a divergence angle of 10 degrees. Journal of the Acoustical Society of America 109, 1616–1630.

Scherer, R.C., Shinwari, D., DeWitt, K.J., Zhang, C., Kucinschi, B.R., Afjeh, A.A., 2002. Intraglottal pressure profiles for a symmetric and oblique glottis with a uniform duct (L). Journal of the Acoustical Society of America 112, 1253–1256.

Scherer, R.C., Torkaman, S., Kucinschi, B.R., Afjeh, A.A., 2010. Intraglottal pressures in a three-dimensional model with a non-rectangular glottal shape. Journal of the Acoustical Society of America 128, 828–838.

Shinwari, D., Scherer, R.C., DeWitt, K.J., Afjeh, A.A., 2003. Flow visualization and pressure distributions in a model of the glottis with a symmetric and oblique divergent angle of 10 degrees. Journal of the Acoustical Society of America 113, 487–497.

Smith, S.L., Thomson, S.L., 2013. Influence of subglottic stenosis on the flow-induced vibration of a computational vocal fold model. Journal of Fluids and Structures 38, 77–91.

Spencer, M., Mongeau, L., Siegmund, T., 2008. Determination of superior-surface strains and stresses, and vocal fold contact pressure in a synthetic larynx model using digital image correlation. Journal of the Acoustical Society of America 123, 1089–1103.

Suh, J., Frankel, S.H., 2007. Comparing turbulence models for flow through a rigid glottal model. Journal of the Acoustical Society of America 123, 1237–1240.

Sváček, P., Horáček, J., 2012. Numerical simulation of glottal flow in interaction with self-oscillating vocal folds: comparison of finite element approximation with a simplified model. Communications in Computational Physics 12, 789–806.

Tallec, P.L., Mouro, J., 2001. Fluid structure interaction with large structural displacements. Computer Methods in Applied Mechanics and Engineering 190, 3039–3067.

Tao, C., Jiang, J.J., 2007. Mechanical stress during phonation in a self-oscillating finite-element vocal fold model. Journal of Biomechanics 40, 2191–2198.

Thomson, S.L., Mongeau, L., Frankel, S.H., 2005. Aerodynamic transfer of energy to the vocal folds. Journal of the Acoustical Society of America 118, 1689–1700.

Titze, I.R., 1994. Mechanical stress in phonation. Journal of Voice 8, 99–105.

Titze, I.R., 2006. The myoelastic aerodynamic theory of phonation. NCVS, Iowa City, Iowa.

Turek, S., Hron, J., 2006. Proposal for numerical benchmarking of fluid-structure interaction between an elastic object and laminar incompressible flow, in: Bungartz, H.J., Schäfer, M. (Eds.), Fluid-Structure Interaction. Springer Berlin Heidelberg. volume 53 of *Lecture Notes in Computational Science and Engineering*, pp. 371–385.

Wittenberg, T., Tigges, M., Mergell, P., Eysholdt, U., 2000. Functional imaging of vocal fold vibration: digital multi-slice high-speed kymography. Journal of Voice 14, 422–442.

Zeitels, S.M., Mauri, M., Dailey, S.H., 2003. Medialization laryngoplasty with Gore-Tex for voice restoration secondary to glottal incompetence: indications and observations. Annals of Otology Rhinology and Laryngology 112, 180.

Zhang, K., Siegmund, T., Chan, R.W., 2009. Modeling of the transient responses of the vocal fold lamina propria. Journal of Mechanical Behavior of Biomedical Materials 2, 93–104.

Zhang, Q., Hisada, T., 2001. Analysis of fluid-structure interaction problems with structural buckling and large domain changes by ale finite element method. Computer Methods in Applied Mechanics and Engineering 190, 6341–6357.

Zhang, Q., Hisada, T., 2004. Studies of strong coupling and weak coupling methods in FSI analysis. International Journal of Numerical Methods in Engineering 60, 2013–2029.

Zhang, Z., 2009. Characteristics of phonation onset in a two-layer vocal fold model. Journal of the Acoustical Society of America 125, 1091–1102.

Zhang, Z., Neubauer, J., Berry, D.A., 2007. Physical mechanisms of phonation onset: A linear stability analysis of an aeroelastic continuum model of phonation. Journal of the Acoustical Society of America 122, 2279–2295.

Zhang, Z., Xuan, Y., 2013. Influence of epithelium and fiber locations on glottal closure and sound production at soft-phonation conditions, in: ICA 2013 Montreal, p. 035045.

Zheng, X., Bielamowicz, S.A., Luo, H., Mittal, R., 2009. A computational study of the effect of false vocal folds on glottal flow and vocal fold vibration during phonation. Annals of Biomedical Engineering 37, 625–642.

Zheng, X., Mittal, R., Xue, Q., Bielamowicz, S., 2011. Direct-numerical simulation of the glottal jet and vocal-fold dynamics in a three-dimensional laryngeal model. Journal of the Acoustical Society of America 130, 404–415.

Zheng, X., Xue, Q., Mittal, R., Bielamowicz, S.A., 2010. A coupled sharp-interface immersed boundary-finite-element method for flow-structure interaction with application to human phonation. Journal of Biomechanical Engineering 132, 111003.